Desalination and Water Treatment
www.deswater.com

doi: 10.5004/dwt.2023.29578

295 (2023) 217–226
May

Multi-response optimization of ultrasound-assisted competitive adsorption of dyes onto γ-Fe_2O_3 nanoparticles loaded on activated carbon: central composite design

Masoumeh Kiani[a,*], Nima Karachi[b], Saideh Bagheri[a,*], Vahid Bagheri[b]

[a]*Department of Chemistry, Payam Noor University, P.O. Box: 19395-3697, Tehran, Iran, emails: M.Kiani@pnu.ac.ir (M. Kiani), S_bagheri2010@yahoo.com (S. Bagheri)*
[b]*Department of Chemistry, Marvdasht Branch, Islamic Azad University, Marvdasht, Iran, emails: nimakarachi@miau.ac.ir (N. Karachi), V_bagheri2020@yahoo.com (V. Bagheri)*

Received 19 August 2022; Accepted 17 April 2023

ABSTRACT

The focus of this study is on the practical use of a reasonable and eco-friendly adsorbent such as γ-Fe_2O_3 nanoparticles loaded on activated carbon (γ-Fe_2O_3-NPs-AC) in fast ultrasound-assisted elimination of Thymol blue (TB) dyes and Azur B (AB) from aqueous solutions. The sorbent was characterized by field-emission scanning electron microscope, X-ray diffraction and Fourier-transform infrared spectroscopy. The effects of pH, sorbent mass, sonication time, eluent volume, and contributions to the response correspond to simultaneous pre-enrichment, determination of TB and AB were optimized by response surface methodology, results were compared with the experimental values. While the superiority of the Langmuir model in explaining the equilibrium data has been demonstrated, pseudo-second-order kinetic equations are well established to describe the adsorption of AB and TB. The high adsorption capacity of the two-component system removes both dyes by more than 99% at high speed (70 mg/g for AB and 45 mg/g for TB) using a small amount of adsorbent. Due to its simplicity and speed, the developed method can successfully perform reproducible and accurate monitoring of analytes of interest from complex matrices.

Keywords: γ-Fe_2O_3 nanoparticles loaded on activated carbon; Response surface methodology; Thymol blue; Azur B; Isotherms; Kinetics

1. Introduction

One of the most serious environmental problems today is pollution. This contamination builds up in living tissue and can cause a variety of disorders and illnesses. Some types of contaminants are highly toxic at relatively low doses [1–7]. Therefore, the focus of theoretical and experimental research is focused on new methods, materials, sensors and catalysts for identifying various pollutants with harmful effects on human health and the environment [8–15]. The direct discharge of industrial wastewater into aquatic media has become an environmental problem, coupled with the difficulty in applying accurate and safe methods of treating such pollutants. Today, environmental researchers and conservationists are concerned about the harmful effects of wastewater containing dyes and pigments [16]. Dyes are considered dangerous and toxic [17,18]. The limitations and shortcomings of conventional adsorbents in removing color even after the overall development of the adsorption system have prompted researchers to improve the adsorption process in a short period of time and use fewer adsorbents to study new adsorbents. and developed [19–23]. In analytical chemistry, Thymol sulfone phthalein, known as Thymol blue (TB) of the triphenylmethane group, exhibits stain-like biological activity. TB dye, as part of a universal indicator, is

* Corresponding authors.

commonly used as a pH indicator. Risks of respiratory irritation, coughing, and shortness of breath have been reported from exposure and inhalation to Thymol blue. Its toxicological properties have not yet been fully investigated, but skin contact causes redness and pain [24]. In the treatment process, the adsorption efficiency can be greatly enhanced by bombarding various reactive sites (OH, COOH, C=O, etc.) of activated carbon and amide groups with nanoparticle characteristics. In this technique, the removal rate and adsorption capacity improvement of AC-based sorbents are directly related to the use of nanoscale high surface area materials. Certain properties such as high mechanical and thermal strength, large number of reactive atoms, large number of free reactive surface sites, highly ordered structure, and metallic or semi-metallic behavior make nanoparticles suitable for a wide variety of applications. It is a good candidate for removal of toxic substances [25,26]. The popularity of ultrasonic irradiation in the acceleration of chemical processes is due to the phenomenon of acoustic cavitation. Acoustic cavitation is defined as the formation and sudden collapse of micrometric bubbles in liquids excited by propagation of a pressure wave [27,28]. Shock waves can generate microscopic turbulence within the interfacial film surrounding adjacent solid particles. Sound waves have the property of creating acoustic streams that provide a driving force that can displace ions and small molecules. In this phenomenon, the conversion of sound into kinetic energy has been noted [29]. Thanks to ultrasound, mass transfer can occur through convective pathways resulting from physical phenomena such as microturbulence, microflow, acoustic (or shock) waves, and microjets, without significantly altering the equilibrium properties of the adsorption/desorption system. can be done. and its secondary effect, "cavitation" (the nucleation, growth, and violent collapse of small gas bubbles [30]). Efficacy has been demonstrated [18,31]. In this article, we report the feasibility of γ-Fe_2O_3 nanoparticles loaded on activated carbon (γ-Fe_2O_3-NPs-AC) as low-cost adsorbents for Azur B (AB) and TB removal from aqueous media. A fast/assisted adsorption method followed by UV detection in the removal of AB and TB was investigated. Central composite design (CCD) combined with RSM (response surface methodology) using DF (desirability function) as the maximization criterion for the response synthesis.

2. Experimental set-up

2.1. Reagents and instruments

The chemical structures of AB (chemical formula $C_{15}H_{16}N_3SCl$)) with a maximum wavelength of 442 nm and TB (chemical formula $C_{27}H_{30}O_5S$) with a maximum wavelength of 650 nm are shown in Fig. 1a and b, respectively. Visible spectra and absorbance measurements were recorded using a UV-visible spectrophotometer (Model Jasco) connected to a personal computer with a 1.0 cm quartz cell. pH was measured using a model 728 pH/ion meter (Metrohm, Switzerland). Application of an ultrasonic bath with a heating system "Tecno-Gaz S.p.A. Ultra Sonic System, Korea" at a frequency of 50 Hz and 296 W helped to disperse the nanoparticles in the solution. All measurements in the study were performed at ambient temperature. An automatic Philips X'Pert X-ray diffractometer (40 kV and 30 mA) from the Netherlands was able to successfully register his X-ray diffraction (XRD) pattern from 20 to over 800 2-h values. All studies on the shape and surface morphology of γ-Fe_2O_3 nanoparticles were performed using his FE-SEM (Hitachi S4160 Field-Emission Scanning Electron Microscope) at an accelerating voltage of 15 kV. The prepared nanoparticles were analyzed for purity using Fourier-transform infrared (FTIR) spectra with a Perkin Elmer Spectrum RX FT-IR spectrometer in the range of 300–4,000 cm^{-1}. The presence of organic and/or other compounds in the prepared nanoparticles was also checked by this method. Preliminary work was done to prepare AB and/or TB stock solutions (100 mg/L), prepared by dissolving 10 mg of each solid dye in 100 mL of double distilled water. Daily preparations of working concentrations were carefully diluted appropriately.

2.2. Simultaneous ultrasonic assisted dye

First, all preparatory work was done to prepare a 50 mL binary dye solution at the correct dye concentration and the solution was prepared. Then, after adjusting the pH of the test solution to 7.0, the solution was poured into a 50 mL Erlenmeyer flask containing 0.03 g of γ-Fe_2O_3-NPs-AC. Ambient temperature was determined as the optimal temperature for all experiments, so we performed at room temperature with the sonication time in the ultrasonic bath set at 4 min. Finally, centrifugal force was used to centrifuge the sample solution and the spectrum of the dye mixture in solution was recorded using a UV-Vis spectrophotometer. It is now possible to calculate the removal rate (*R*%AB and *R*%TB) of each dye and the adsorption capacity (q_t, mg/g) of each dye using the following formulas:

$$\%\ \text{dye removal} = \frac{\left(C_0 - C_t\right)}{C_0} \times 100 \tag{1}$$

where C_0 (mg/L) denotes the target concentration at the initial time and C_t (mg/L) denotes the target concentration after time *t*.

$$q_e = \frac{\left(C_0 - C_e\right)V}{W} \tag{2}$$

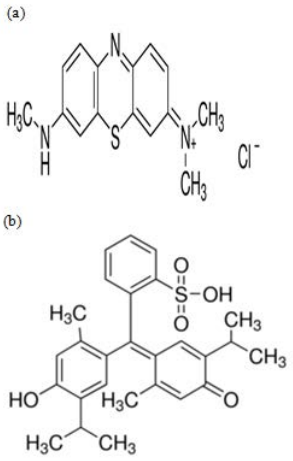

Fig. 1. (a) Chemical structures of Azur B and (b) Thymol blue.

where C_0 (mg/L) is an index of the initial dye concentration and C_e (mg/L) is the equilibrium dye concentration in aqueous solution. The volume of the solution is denoted V (L) and the mass of the adsorbent is denoted W (g).

2.3. Synthesis of γ-Fe_2O_3-NPs-AC

The Chem-Lab Company kindly provided the activated carbon used as support for the prepared γ-Fe_2O_3-NPs-AC. We also prepared a reaction solution for loading γ-Fe_2O_3-NPs-AC nanoparticles onto activated carbon (AC) by following the procedure. First, 0.018 mmol of ferrous sulfate solution and 0.021 mmol of $NH_4Fe(SO_4)_2{\cdot}12H_2O$ were dissolved in deionized water using 6 mL of concentrated sulfuric acid solution, and then deionized water was added to make up the total volume. 150 mL. Mix the prepared solution with 20.0 g of activated carbon in an Erlenmeyer flask. After that, the Erlenmeyer flask was placed under a magnetic mixer, and droplets of sodium hydroxide (140 mL of 1.5 M) were gradually added to the prepared mixed solution at room temperature over 70 min. The resulting solution was stirred at ambient temperature for 17 h. After 17 h, caustic soda (3 M 100 mL) was gradually added dropwise to the reaction solution at room temperature over 40 min, and the prepared reaction solution was again vigorously stirred at 100°C for 4 h using a magnetic stirrer. room temperature. The γ-Fe_2O_3-NPs-AC provided was filtered and rinsed several times with distilled water. Finally, the provided γ-Fe_2O_3-NPs-AC was dried at 35°C for 15 h for use as absorbent in adsorption experiments.

2.4. Statistical analysis

Using CCD or central composite design as the most common type of RSM, AB (*A*) and TB (*B*) dye concentration, pH (*C*), adsorbent amount (*D*), and contact time (*E*) explained the γ-Fe_2O_3 effect of and optimize. On ultrasound-assisted adsorption of AB and TB dyes by γ-Fe_2O_3. Based on what is presented in Tables 1 and 2, the *R*% for AB and TB dyes was calculated according to 5 independent variables set at 5 levels. Analysis of variance (ANOVA) has been used successfully [32,33] to identify key strong conditions for modeling responses based on *F*-tests and *p*-values.

3. Findings and discussion

3.1. Characterisation of adsorbent

As shown in Fig. 2a, FE-SEM images of γ-Fe_2O_3-NPs revealed uniformity, fineness, and roundness of particles with diameters less than 50 nm. The γ-Fe_2O_3-NP particles show good shape and size uniformity. A SEM image of the prepared γ-Fe_2O_3-NPs-AC is shown in Fig. 2b. This indicates to some extent the porosity of this material. The XRD in Fig. 3a analyzes the structure of γ-Fe_2O_3-NPs and shows that the signals at 2θ = 30.1°, 35.7°, 57.1° and 62.7° belong to the (100) lattice plane. I was (002), (101), (102), and (110), confirming the block structure of the γ-Fe_2O_3 nanoparticles. The prominent XRD signals in Fig. 3 served as an indication of the well-crystallized structure of the provided γ-Fe_2O_3-NPs, but the presence of Fe, $Fe(OH)_2$, $Fe(OH)_3$ and/or other compounds. There were no signals related to impurities agreed or any other connection. The Debye–Scherrer equation calculated an approximate nanocrystallite size of 13 nm for the prepared γ-Fe_2O_3 particles. Also, the FWHM (full width at half maximum) of the (311) signal provides more data on size. Fig. 3b shows X-ray powder diffraction patterns of Fe_2O_3-NPs-AC (JCPDS. NO. 01-075-0033) over 2 h ranges from 20 to 80, it was found that there were a series of characteristic peaks at (220), (311), (222), (400), (422), (511), (440), (620), (533) and (444). The FTIR spectra of the prepared γ-Fe_2O_3-NPs were recorded in the range of 300–4,000 cm^{-1}, as shown in Fig. 4a. A sharp bond at 345 cm^{-1} is proportional to the Fe–O bonding and a broad absorption bond at 529 cm^{-1} contributes to the Fe–O stretching mode of γ-Fe_2O_3-NPs [34]. The visible signal in the range 1,500–3,500 cm^{-1} is proportional to water molecules absorbed in the KBr matrix or γ-Fe_2O_3 nanoparticles. Presumably, the vibrational mode of C=O absorbed on the surface of γ-Fe_2O_3-NPs gave rise to the visible signal at 1,100 cm^{-1}. From the FTIR data, there is no evidence that the γ-Fe_2O_3-NPs nanoparticles were contaminated by unknown substances in the system. However, further phase confirmation by FTIR analysis (Fig. 4b) reveals a sharp absorption peak at 570.34 cm corresponding to vibrations of the Fe–O bonding properties of γ-Fe_2O_3-NPs. There is another absorption band between 3,250 and 3,750 cm^{-1}, which is attributed to the stretching of hydroxyl groups (–OH) present in KBr due to adsorption of atmospheric moisture. These analyzes confirm that the Fe_2O_3-NPs consist of pure-phase magnetite.

3.2. Analysis of CCD

As detailed in Table 3, data on the leading variables and their feasible interactions were obtained using ANOVA. Based upon the *F*-value of 18.88 for AB and 18.98 for TB in this model and the small *p*-values (<0.0001) for the phases as well, the model was considered suitable and applicable in

Table 1
Experimental factors and levels in the central composite design

Factors	Levels			Star point α = 2.37	
	Low (–1)	Central (0)	High (+1)	–α	+α
(*A*) concentration (mg/L)	6	10	14	2	18
(*B*) concentration (mg/L)	8	12	16	4	20
(*C*) pH	2	6	10	2	10
(*C*) adsorbent (g)	0.02	0.025	0.030	0.015	0.035
(*D*) Time (min)	3	4	5	2	6

Table 2
Experimental conditions and values obtained through the central composite design

Runs	*A*	*B*	*C*	*D*	*E*	AB removal (%)	TB removal (%)
1	14	8	4	0.03	5	82.24	99.8
2	6	16	8	0.02	3	89.49	90.86
3	6	8	8	0.03	3	95.6	99.03
4	6	16	8	0.02	5	99.54	96.49
5	14	8	4	0.02	5	66	97.87
6	14	16	8	0.02	5	71.82	90.44
7	14	16	4	0.02	5	75	87.65
8	14	16	8	0.02	3	71	88.74
9	10	12	6	0.035	4	96.79	99.66
10	6	8	8	0.02	5	84.87	99.25
11	10	12	2	0.025	4	83.85	96.64
12	10	12	6	0.015	4	79.35	89.2
13	14	8	8	0.02	5	59	99.51
14	14	8	4	0.03	3	78.7	99.51
15	10	12	6	0.025	4	89.1	98.45
16	14	16	4	0.02	3	73	85
17	14	8	4	0.02	3	60.51	97.49
18	6	16	8	0.03	5	95.43	98.83
19	14	8	8	0.03	5	88.07	99.9
20	14	16	4	0.03	3	87.53	94.64
21	6	16	8	0.03	3	95.89	98.57
22	14	16	4	0.03	5	88.31	95.24
23	10	12	6	0.025	4	92.5	99.11
24	14	8	8	0.03	3	80.73	99.8
25	6	8	8	0.03	5	97.56	99.62
26	10	12	10	0.025	4	85.48	99.79
27	10	20	6	0.025	4	88.92	96.11
28	10	12	6	0.025	4	87.78	98.18
29	6	8	4	0.03	3	91.5	100
30	6	8	8	0.02	3	88.78	98.21
31	14	16	8	0.03	3	90.42	98.65
32	2	12	6	0.025	4	100	99.62
33	10	12	6	0.025	2	81.56	90.75
34	14	8	8	0.02	3	55	99.31
35	6	16	4	0.02	3	83.75	88.98
36	6	16	4	0.02	5	87.71	90
37	6	8	4	0.02	5	90.84	95.44
38	10	12	6	0.025	4	85	96.43
39	10	12	6	0.025	4	90.75	98.85
40	6	8	4	0.03	5	98.35	98.76
41	18	12	6	0.025	4	74.24	98.59
42	10	12	6	0.025	4	86.87	98.11
43	6	16	4	0.03	3	96.44	98.31
44	10	12	6	0.025	6	86	94.15
45	6	8	4	0.02	3	88.23	94.25
46	6	16	4	0.03	5	90	96.08
47	10	12	6	0.025	4	83.82	97.14
48	14	16	8	0.03	5	81.99	98.02
49	10	4	6	0.025	4	80	99.23
50	10	12	6	0.025	4	91.58	98

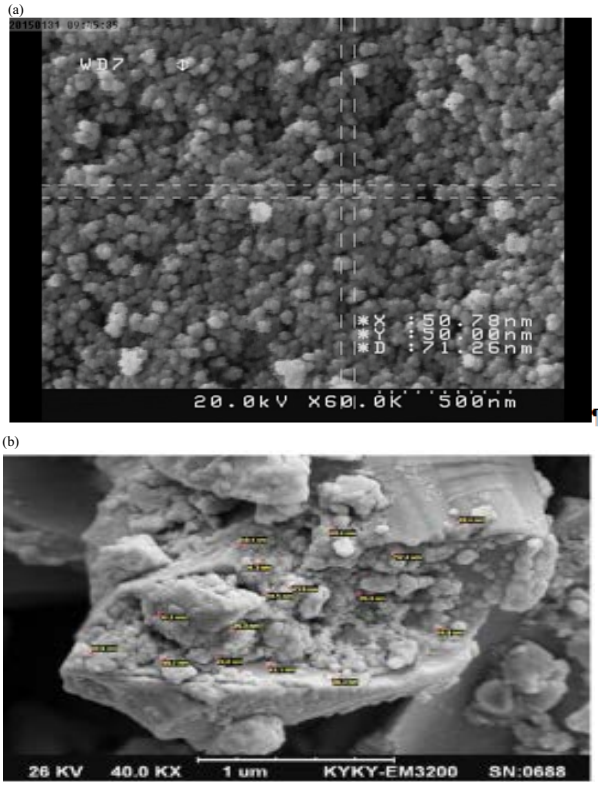

Fig. 2. (a) Field-emission scanning electron microscope image of the prepared γ-Fe_2O_3-NPs and (b) scanning electron microscope image of the γ-Fe_2O_3-NPs-AC adsorbent.

anticipating AB and TB elimination within 95% confidence level. Also, the appropriateness of this model in anticipating experimental data was highly proven from "Lack of Fit *F*-value" of 1.4 for AB and 2.75 for TB and the corresponding *p*-value as well. Finally, the model was highly considered applicable in anticipating the removal percentage of AB and TB by looking at the values of the determination coefficient R^2 for AB (0.97) and TB (0.98) and the adjusted R^2 for AB (0.95) and TB (0.96). Thus, to model the removal percentage (R%) of for AB and TB, the ensuing semi-empirical expression was applied:

$$\begin{aligned} R\%_{AB} &= 82.144 - 8.4724A + 4.0654B - 0.034625C \\ &+ 7.8972D + 3.7386E + 2.0719AB - 1.0500AC \\ &+ 3.0969AD + 0.028750AE + 0.64375BC \\ &- 1.4006BD - 0.8BE + 0.56750CD - 0.23187CE \\ &- 0.62125DE - 0.53913A^2 - 1.2041B^2 - 1.1529C^2 \\ &- 0.30162D^2 - 1.3741E^2 \end{aligned} \quad (3)$$

$$\begin{aligned} R\%_{TB} &= 96.107 - 0.0088750A - 2.1617B - 0.83884C \\ &+ 2.9668D + 3.1910E - 0.88656AB - 0.058438AC \\ &+ 0.11969AD - 0.030312AE + 0.41219BC \\ &+ 1.4091BD + 0.20156BE - 0.50156CD + 0.19469CE \\ &- 0.50219DE + 0.29006A^2 - 0.068688B^2 + 0.067563C^2 \\ &- 0.87869D^2 - 1.3737E^2 \end{aligned} \quad (4)$$

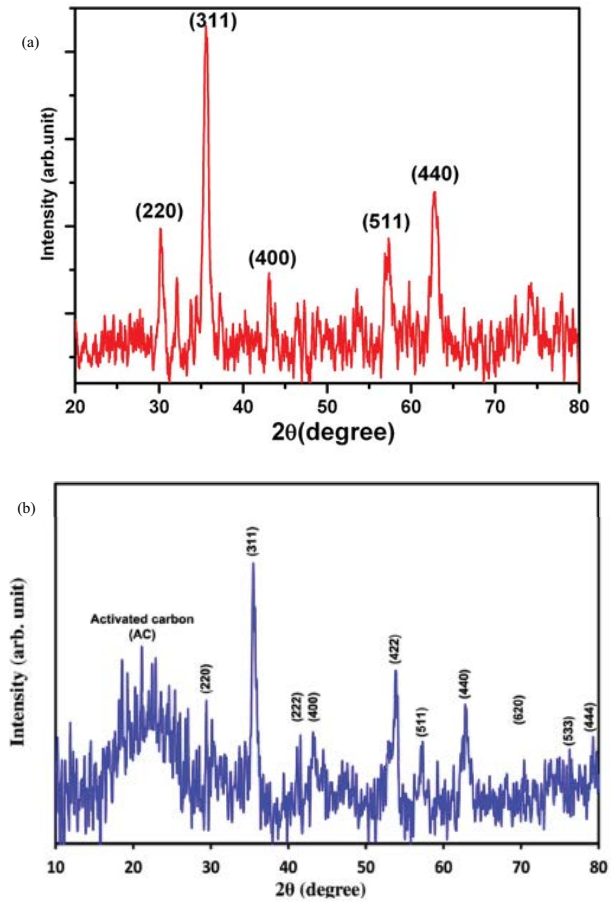

Fig. 3. X-ray diffraction pattern of (a) prepared γ-Fe_2O_3-NPs and (b) Fe_2O_3-NPs-AC.

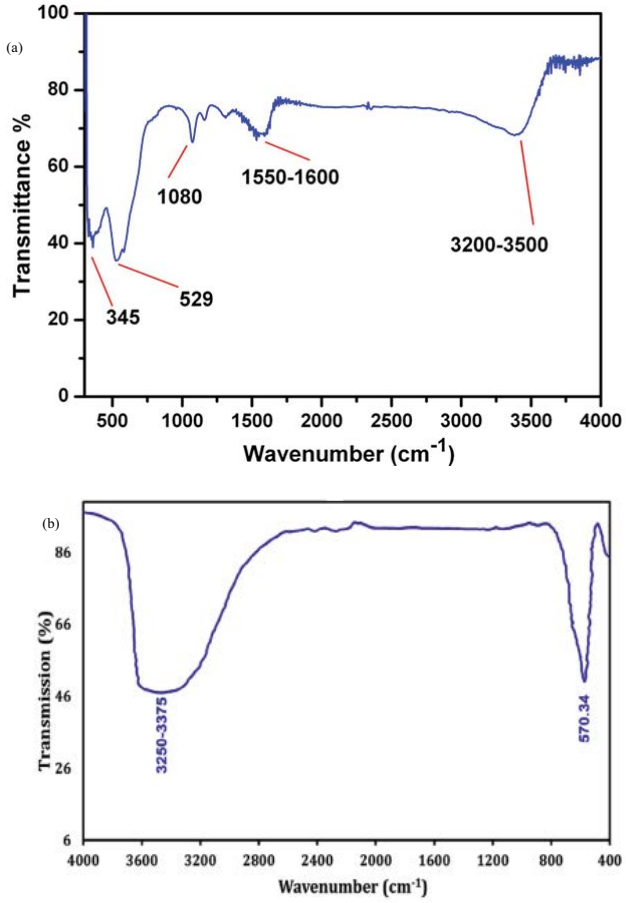

Fig. 4. (a) Fourier-transform infrared transmittance spectrum of the prepared γ-Fe_2O_3-NPs and (b) Fourier-transform infrared spectra of γ-Fe_2O_3-NPs-AC.

3.3. Optimization condition

The desirability profiles detailing the desired removal rates for the AB and TB dyes are shown in Fig. 5. Preferred values of 1.0, 0.5, and 0.0 correspond to maximum (100% and 100%), minimum (55% and 85%), and average (77.5% and 92.5%) of AB or TB. In the diagram above (Fig. 5), the responses are displayed in the top right and the individual desirability values are displayed in the left (bottom). The final response obtained from these plots using the current level of each variable in the model when the target desirability value is set to 1.0 is shown in Fig. 5 above (left). The optimized conditions are 4 min (sonication time), 7 (pH), 0.03 g (adsorbed amount), (AB dye concentration) is 6 mg/L, and TB dye concentration is 10.5 mg/L.

3.4. Response surface plots

Remarkable interactions of variables and their impacts on the CCD were assessed through applying response surface plots. (Fig. 6a), adsorbent dosage is vital in increasing removal efficiency and any change in initial dye concentration can directly be related to adsorbent dose. The fact that the significant increase in adsorption efficiency was due to the increase in adsorbent dose was evident and related highly to more available surface area for adsorption. The state that removal percentage remarkably diminished at lower amount of adsorbent was explainable in this way that the ratio of dye molecules compare to vacant site of adsorbent was higher. The significant interaction effect of initial dye concentration on its removal percentage is shown in Fig. 6b gave rise to reduction in removal percentage. This is explainable in this way that the ratio of dye molecule to available surface area for adsorption increased. Fig. 6c details the alterations in the percentage removal as a function of sonication time. Removal percentage had a positive correlation with sonication time (increase–increase). According to this figure, the maximum dye adsorption was achieved at sonication time of 4 min. Fig. 6d shows the effects of initial AB concentration and pH on the adsorption of AB dye onto γ-Fe_2O_3-NPs-AC. Keeping the pH fixed, the adsorption of AB increased with the decrease of initial dye concentration. Inversely, pH caused an initial increase in the adsorption of AB. The most favorable adsorption of AB dye (97.87%) was seen at basic pH 6–10 (Fig. 6d). At lower pH, the number of positively charged adsorbent surface sites increases. Consequently, electrostatic repulsion between the positively charged surface and the positively charged dye molecules increases with increasing solution pH, which decreases the adsorption efficiency of AB. In addition, the

Table 3
Analysis of variance for response surface quadratic model

Source of variation	AB					TB				
	SS[a]	DF[b]	MS[c]	*F*-value	*p*-value	SS	df	MS	*F*-value	*p*-value
Model	4,813	20	240.65	18.88	<0.0001	682.04	20	34.102	18.987	<0.0001
A	820.36	1	820.36	64.36	<0.0001	0.0009	1	0.0009	0.00050	0.98229
B	257.99	1	257.99	20.241	0.000102	125.2	1	125.2	69.71	<0.0001
C	0.018714	1	0.018714	0.001468	0.9697	10.984	1	10.984	6.1156	0.019503
D	973.51	1	973.51	76.376	<0.0001	137.39	1	137.39	76.498	<0.0001
E	88.569	1	88.569	6.9486	0.013332	64.521	1	64.521	35.924	<0.0001
AB	137.37	1	137.37	10.777	0.002683	25.152	1	25.152	14.004	0.000802
AC	35.28	1	35.28	2.7679	0.10695	0.10928	1	0.10928	0.06084	0.80691
AD	306.9	1	306.9	24.078	<0.0001	0.4584	1	0.4584	0.25523	0.61723
AE	0.02645	1	0.02645	0.002075	0.96398	0.02940	1	0.02940	0.01637	0.89907
BC	13.261	1	13.261	1.0404	0.31616	5.4368	1	5.4368	3.0271	0.09249
BD	62.776	1	62.776	4.925	0.034451	63.535	1	63.535	35.375	<0.0001
BE	20.48	1	20.48	1.6067	0.21503	1.3001	1	1.3001	0.72386	0.40185
CD	10.306	1	10.306	0.80853	0.37596	8.0501	1	8.0501	4.4821	0.04295
CE	1.7205	1	1.7205	0.13498	0.71599	1.2129	1	1.2129	0.67532	0.41791
DE	12.35	1	12.35	0.96895	0.33309	8.0702	1	8.0702	4.4933	0.042709
A^2	9.301	1	9.301	0.7297	0.39998	2.6924	1	2.6924	1.499	0.23067
B^2	46.397	1	46.397	3.6401	0.06635	0.15098	1	0.15098	0.08406	0.77393
C^2	0.14607	1	0.14607	0.081329	0.77753	0.14607	1	0.14607	0.08132	0.77753
D^2	2.9113	1	2.9113	0.2284	0.63629	24.707	1	24.707	13.756	0.000876
E^2	60.423	1	60.423	4.7404	0.037743	60.385	1	60.385	33.621	<0.0001
Residual	52.085	29	1.7960			52.085	29	1.796		
Lack of fit	301.45	22	13.702	1.4066	0.33661	46.688	22	2.1222	2.7525	0.086168
Pure error	68.192	7	9.7417			5.397	7	0.771		
Cor total	5,182.7	49				734.13	49			

[a]sum of square;
[b]degree freedom;
[c]mean square.

competition of H^+ ions with the cationic dye molecules decreases the adsorption efficiency. The surface of the adsorbent was negatively charged at higher pH, which favored for the adsorption of the positively charged dye cations through electrostatic attraction force. Consequently, the adsorption of AB increases with increasing pH values.

3.5. Adsorption isotherms study

Adsorption isotherms provide information about how adsorption systems work and how effectively a particular adsorbent can interact with an adsorbate [34]. A number of isothermal models have been developed for evaluation and used to analyze equilibrium adsorption. Among them, Langmuir [35], Freundlich [36], Redlich–Peterson [37], Temkin [38], Dubinin–Radushkevich [39] design and optimization models of adsorption processes are known. In the traditional linear form, we analyzed the slope and intercept of each line to confirm their invariance (Table 4). According to this table, the R^2 of the Langmuir model is higher than the other isotherms for the adsorption of both dyes studied, which suggests that the Langmuir adsorption isotherms are more sensitive to the adsorption of AB and TB on γ-Fe_2O_3-NPs. It means that it represents exactly. Alternating current. This indicates that the adsorption occurs as monolayer deposition of the dye onto γ-Fe_2O_3-NPs-AC. The maximum adsorption capacities of AB and TB on γ-Fe_2O_3 nanoparticles supported on activated carbon are 70 and 45 mg/g, respectively.

3.6. Adsorption kinetic model

Numerous parameters related to the solid state and the physical and chemical conditions under which sorption occurs can strongly control the kinetics of the adsorption process. Evaluation of the adsorption process of AB and TB dyes onto adsorbents was performed using different models including Elovich, pseudo-first-order, pseudo-second-order and intraparticle diffusion models [40–43]. All parameters were accurately calculated using plots of the kinetic model equations (Table 5). The principles and criteria by which the applicability of these models was determined were based on evaluation of their respective correlation coefficients (R^2) and agreement between experimental and calculated values of q_e. Considering the high values of R^2 (0.997 and 0.999)

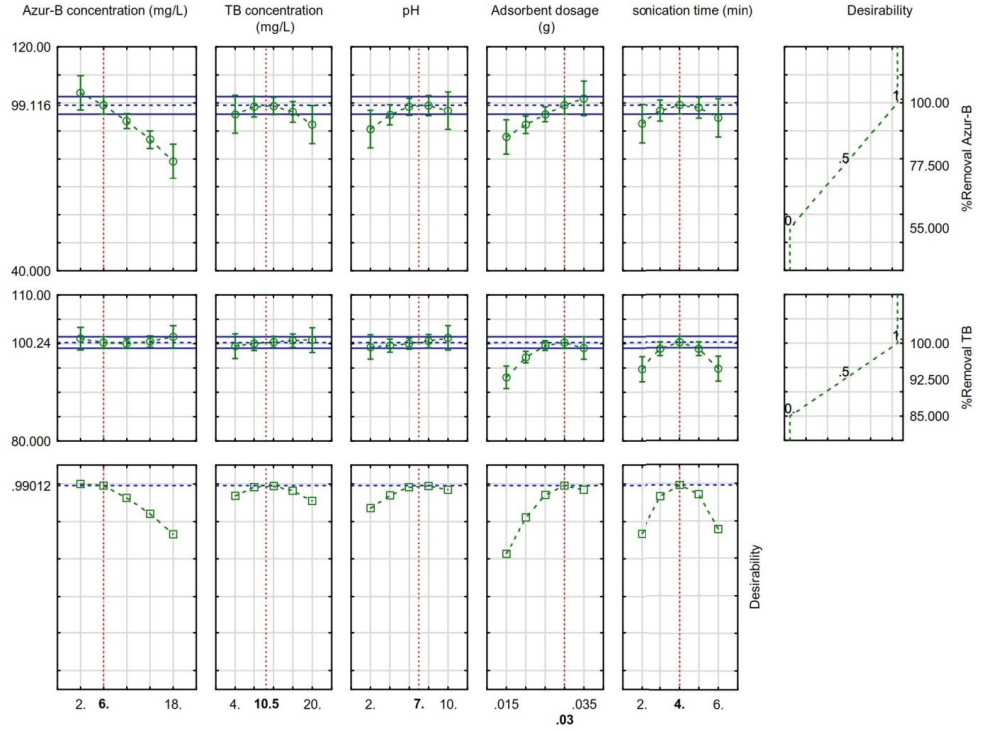

Fig. 5. Profile for predicted values and desirability function for removal percentage of AB and TB dyes.

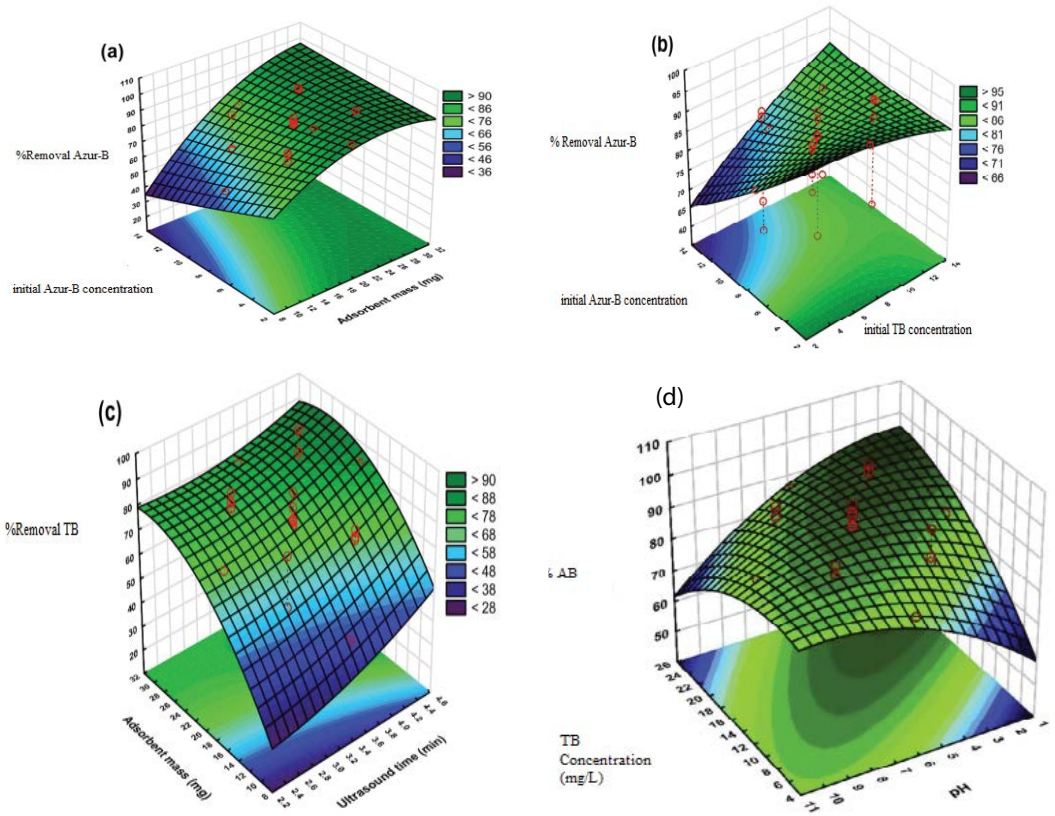

Fig. 6. Response surfaces for the dyes removal: (a) initial Azur B concentration – adsorbent mass, (b) initial Azur B concentration – initial TB concentration, (c) adsorbent mass – ultrasound time, and (d) initial TB concentration – pH.

Table 4
Various isotherm constants and their correlation coefficients calculated for the adsorption of AB and TB onto γ-Fe_2O_3-NPs-AC

Isotherm	Equation	Parameters	Value of parameters for AB	Value of parameters for TB
Langmuir	$q_e = q_m bC_e/(1 + bC_e)$	q_m (mg/g)	70	45
		K_a (L/mg)	40	4
		R^2	98.36	98.43
Freundlich	$\ln q_e = \ln K_F + (1/n)\ln C_e$	$1/n$	0.8035	0.806
		K_F (L/mg)	8.17	8.18
		R^2	95	96
Temkin	$q_e = B_1 \ln K_T + B_1 \ln C_e$	B_1	12	8
		K_T (L/mg)	4,707.6	1,113.6
		R^2	82	96
Dubinin–Radushkevich	$\ln q_e = \ln Q_s - B\varepsilon^2$	Q_s (mg/g)	59.02	37
		B	–11E-08	–4.2E-07
		E (kJ/mol)	11E+03	10E+03
		R^2	0.76	0.87

Table 5
Various kinetic constants and their correlation coefficients calculated for the adsorption of AB and TB onto γ-Fe_2O_3-NPs-AC

Model	Parameters	Value of parameters for AB	Value of parameters for TB
Pseudo-first-order kinetic	k_1 (min^{-1})	1.50	2.13
	q_e (calc) (mg/g)	9.54	7.4
	R^2	98	97.46
Pseudo-second-order kinetic	k_2 (min^{-1})	2.24E-03	2.65E-03
	q_e (calc) (mg/g)	31.718	52.76
	R^2	99.7	99.93
Intraparticle diffusion	K_{diff} (mg/g·$min^{-1/2}$)	4.65	3.2
	C (mg/g)	19.16	45.35
	R^2	96.56	96.59
Elovich	β (g/mg)	3.85	2.512
	α (mg/g·min)	31E+03	134E-03
	R^2	96.6	98.27

and the good agreement between the two q_e values, it was clear that this adsorption system followed a pseudo-second-order kinetics model. It was assumed that the limiting step could lead the process to a chemisorption process. The constancy of the secondary adsorption rate (k_2) in this model decreased with increasing equilibrium adsorption time.

3.7. Regeneration of γ-Fe_2O_3-NPs-AC

To make the process more economical and viable, the material was regenerated and the economics of the process were greatly improved. After adsorption, γ-Fe_2O_3-NPs-AC was regenerated by repeated washing with a small amount of acetonitrile. Fig. 1 shows the reproduction characteristics of each colorant. The adsorption of AB and TB decreased gradually with increasing desorption cycles, but the regenerated γ-Fe_2O_3-NPs-AC still shows good performance for their adsorption. After the 6th cycle of desorption, the sorption

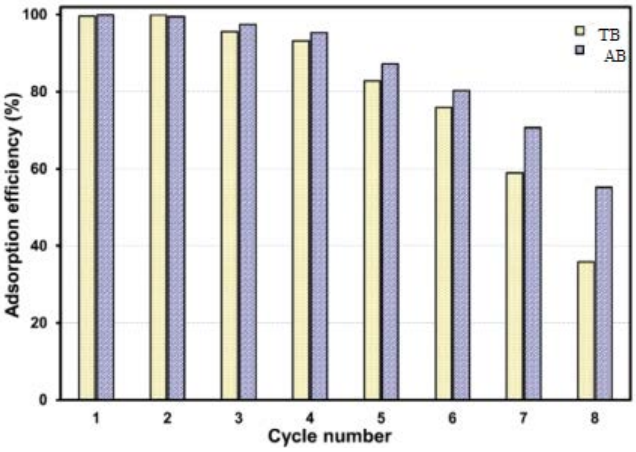

Fig. 7. Effect of regeneration cycles on the ultrasound-assisted simultaneous adsorption of TB and AB onto γ-Fe_2O_3-NPs-AC.

amounts of TB and AB by γ-Fe_2O_3-NPs-AC reached 82% and 76% of that of the fresh material, respectively.

4. Conclusion

In this article, γ-Fe_2O_3-NPs-AC were prepared by a simple method and identified by FE-SEM, FTIR and XRD analyses. The effects of parameters such as sample pH, sonication time, amount of adsorbent, AB and TB concentrations on the reaction were investigated. The desirability functions show that the optimal distances (99.1% for AB and 99.8% for TB) were achieved under the previously specified best operating conditions. Although the kinetic and isotherm data were described by the pseudo-quadratic and Langmuir models, the maximum adsorption capacities for AB and TB assigned to the Langmuir model were 70 and 45 for 0.03 g γ-Fe_2O_3-NPs-AC, respectively for 0.03 g γ-Fe_2O_3-NPs-AC at 25°C. The optimized method was successfully applied to real wastewater samples. Furthermore, the results of this study will help researchers and industry to more efficiently exploit the advantages of ultrasonic devices in dye adsorption. It is worth noting that applying the optimized method to real wastewater samples yielded positive results.

Acknowledgment

The authors gratefully acknowledge the financial support from the Payame Noor University, Branch of Busher, Iran.

References

[1] M. Masoudzadeh, N. Karachi, Removal of cadmium ion from wastewater using carboxylated nanoporous graphene (G-COOH), Eurasian J. Anal. Chem., 13 (2018) 1–10, doi: 10.29333/ejac/90596.
[2] M. Kiani, S. Bagheri, N. Karachi, E. Alipanahpour Dil, Adsorption of purpurin dye from industrial wastewater using Mn-doped Fe_2O_4 nanoparticles loaded on activated carbon, Desal. Water Treat., 152 (2019) 366–373.
[3] P. Nasehi, M. Saei Moghaddam, S.F. Abbaspour, N. Karachi, Preparation and characterization of a novel Mn-Fe_2O_4 nanoparticle loaded on activated carbon adsorbent for kinetic, thermodynamic and isotherm surveys of aluminum ion adsorption, Sep. Sci. Technol., 55 (2020) 1078–1088.
[4] M.R. Parvizi, N. Karachi, Isotherm and kinetic study of disulfin blue and methyle orange dyes by adsorption onto by titanium dioxide-NPs loaded onto activated carbon: experimental design, Orient. J. Chem., 33 (2017) 2559–2565.
[5] N. Karachi, Enhanced removal of humic acids (HAs) from aqueous solutions using MWCNTs modified by N-(3-nitrobenzylidene)-N-trimethoxysilylpropyl-ethane-1,2-diamine on equilibrium, thermodynamic and kinetics, J. Phys. Theor. Chem., 14 (2017) 259–270.
[6] M. Kiani, S. Bagheri, A. Khalaji, N. Karachi, Ultrasonic supported deletion of Rhodamine B on ultrasonically synthesized zinc hydroxide nanoparticles on activated carbon concocted from wood of cherry tree: experimental design methodology and artificial neural network, Desal. Water Treat., 226 (2021) 147–156.
[7] N. Karachi, S. Motahari, S. Nazarian, Working for the betterment of simultaneous deletion of paraben dyes from industrial effluents on to *Origanum majorana*-capped silver nanoparticles, Desal. Water Treat., 228 (2021) 389–402.
[8] N. Karachi, O. Azadi, R. Razavi, A. Tahvili, Z. Parsaee, Combinatorial experimental and DFT theoretical evaluation of a nano novel thio-dicarboxaldehyde based Schiff base supported on a thin polymer film as a chemosensor for Pb^{2+} detection, J. Photochem. Photobiol., A, 360 (2018) 152–165.
[9] Z. Parsaee, N. Karachi, R. Razavi, Ultrasound-assisted fabrication of a novel optode base on a triazine based Schiff base immobilized on TEOS for copper detection, Ultrason. Sonochem., 47 (2018) 36–46.
[10] M. Sarafbidabad, Z. Parsaee, Z. Noor Mohammadi, N. Karachi, R. Razavi, Novel double layer film composed of reduced graphene oxide and Rose Bengal dye: design, fabrication and evaluation as an efficient chemosensor for silver(I) detection, New J. Chem., 42 (2018) 13674–13683.
[11] Z. Parsaee, N. Karachi, S.M. Abrishamifar, M.R.R. Kahkha, R. Razavi, Silver-choline chloride modified graphene oxide: novel nano-bioelectrochemical sensor for celecoxib detection and CCD-RSM model, Ultrason. Sonochem., 45 (2018) 106–115.
[12] N. Karachi, M. Hosseini, Z. Parsaee, R. Razavi, Novel high performance reduced graphene oxide based nanocatalyst decorated with Rh_2O_3/Rh-NPs for CO_2 photoreduction, J. Photochem. Photobiol., A, 364 (2018) 344–354.
[13] L. Zhou, H. Kamyab, A. Surendar, A. Maseleno, A.Z. Ibatova, S. Chelliapan, N. Karachi, Z. Parsaee, Novel Z-scheme composite Ag_2CrO_4/NG/polyimide as high performance nano catalyst for photoreduction of CO_2: design, fabrication, characterization and mechanism, J. Photochem. Photobiol., A, 368 (2019) 30–40.
[14] N. Karachi, M. Emadi, M. Servatkhah, Computational investigation on structural properties of carbon nanotube binding to nucleotides according to the QM methods, J. Optoelectron. Nanostruct., 4 (2019) 99–124.
[15] M. Monajjemi, N. Karachi, F. Mollaamin, The investigation of sequence-dependent interaction of messenger RNA binding to carbon nanotube, Fullerenes Nanotubes Carbon Nanostruct., 22 (2014) 643–662.
[16] A. Asfaram, M. Ghaedi, S. Agarwal, I. Tyagi, V.K. Gupta, Removal of basic dye Auramine-O by ZnS:Cu nanoparticles loaded on activated carbon: optimization of parameters using response surface methodology with central composite design, RSC Adv., 5 (2015) 18438–18450.
[17] A. Asfaram, M. Ghaedi, S. Hajati, A. Goudarzi, Ternary dye adsorption onto MnO_2 nanoparticle-loaded activated carbon: derivative spectrophotometry and modeling, RSC Adv., 5 (2015) 72300–72320.
[18] A. Sarı, M. Tuzen, Biosorption of total chromium from aqueous solution by red algae (*Ceramium virgatum*): equilibrium, kinetic and thermodynamic studies, J. Hazard. Mater., 160 (2008) 349–355.
[19] O.D. Uluozlu, A. Sari, M. Tuzen, M. Soylak, Biosorption of Pb(II) and Cr(III) from aqueous solution by lichen (*Parmelina tiliaceae*) biomass, Bioresour. Technol., 99 (2008) 2972–2980.
[20] R.A. Anayurt, A. Sari, M. Tuzen, Equilibrium, thermodynamic and kinetic studies on biosorption of Pb(II) and Cd(II) from aqueous solution by macrofungus (*Lactarius scrobiculatus*) biomass, Chem. Eng. J., 151 (2009) 255–261.
[21] A. Sari, D. Mendil, M. Tuzen, M. Soylak, Biosorption of Cd(II) and Cr(III) from aqueous solution by moss (*Hylocomium splendens*) biomass: equilibrium, kinetic and thermodynamic studies, Chem. Eng. J., 144 (2008) 1–9.
[22] A. Sarı, M. Tuzen, Kinetic and equilibrium studies of biosorption of Pb(II) and Cd(II) from aqueous solution by macrofungus (*Amanita rubescens*) biomass, J. Hazard. Mater., 164 (2009) 1004–1011.
[23] S.-Y. Jeong, J.-W. Lee, Optimization of pretreatment condition for ethanol production from oxalic acid pretreated biomass by response surface methodology, Ind. Crops Prod., 79 (2016) 1–6.
[24] M. Ghaedi, Sh. Heidarpour, S. Nasiri Kokhdan, R. Sahraie, A. Daneshfar, B. Brazesh, Comparison of silver and palladium nanoparticles loaded on activated carbon for efficient removal of Methylene blue: kinetic and isotherm study of removal process, Powder Technol., 228 (2012) 18–25.
[25] M. Ghaedi, K. Niknam, S. Zamani, H. Abasi Larki, M. Roosta, M. Soylak, Silica chemically bonded *N*-propyl kriptofix 21 and 22 with immobilized palladium nanoparticles for solid phase extraction and preconcentration of some metal ions, Mater. Sci. Eng., C, 33 (2013) 3180–3189.

[26] A.R. Abbasi, K. Akhbari, A. Morsali, Dense coating of surface mounted CuBTC metal-organic framework nanostructures on silk fibers, prepared by layer-by-layer method under ultrasound irradiation with antibacterial activity, Ultrason. Sonochem., 19 (2012) 846–852.
[27] S. Khanjani, A. Morsali, Ultrasound-promoted coating of MOF-5 on silk fiber and study of adsorptive removal and recovery of hazardous anionic dye "Congo red", Ultrason. Sonochem., 21 (2014) 1424–1429.
[28] M. Jamshidi, M. Ghaedi, K. Dashtian, S. Hajati, New ion-imprinted polymer-functionalized mesoporous SBA-15 for selective separation and preconcentration of Cr(III) ions: modeling and optimization, RSC Adv., 5 (2015) 105789–105799.
[29] M. Jamshidi, M. Ghaedi, K. Dashtian, S. Hajati, A. Bazrafshan, Ultrasound-assisted removal of Al^{3+} ions and Alizarin red S by activated carbon engrafted with Ag nanoparticles: central composite design and genetic algorithm optimization, RSC Adv., 5 (2015) 59522–59532.
[30] E.A. Dil, M. Ghaedi, A. Asfaram, A. Goudarzi, Synthesis and characterization of ZnO-nanorods loaded onto activated carbon and its application for efficient solid phase extraction and determination of BG from water samples by micro-volume spectrophotometry, New J. Chem., 39 (2015) 9407–9414.
[31] Y. Liu, G. Cui, C. Luo, L. Zhang, Y. Guo, S. Yan, Synthesis, characterization and application of amino-functionalized multi-walled carbon nanotubes for effective fast removal of methyl orange from aqueous solution, RSC Adv., 4 (2014) 55162–55172.
[33] A. Goudarzi, A. Dorbeygi Namghi, C.-S. Ha, Fabrication and characterization of nano-structured ZnS thin films as the buffer layers in solar cells, RSC Adv., 4 (2014) 59764–59771.
[34] S.K. Sahoo, K. Agarwal, A.K. Singh, B.G. Polke, K.C. Raha, Characterization of γ- and α-Fe_2O_3 nano powders synthesized by emulsion precipitation-calcination route and rheological behaviour of α-Fe_2O_3, Int. J. Eng. Sci. Technol., 2 (2010) 118–126.
[35] M. Arshadi, A.R. Faraji, M. Mehravar, Dye removal from aqueous solution by cobalt-nano particles decorated aluminum silicate: kinetic, thermodynamic and mechanism studies, J. Colloid Interface Sci., 440 (2015) 91–101.
[36] T.A. Khan, S. Sharma, I. Ali, Adsorption of Rhodamine B dye from aqueous solution onto acid activated mango (*Magnifera indica*) leaf powder: equilibrium, kinetic and thermodynamic studies, J. Toxicol. Environ. Health Sci., 3 (2011) 286–297.
[37] Y.E. Unsal, M. Soylak, M. Tuzen, Dispersive liquid–liquid microextraction–spectrophotometry combination for determination of rhodamine B in food, water, and environmental samples, Desal. Water Treat., 55 (2015) 2103–2108.
[38] P.S. Ardekani, H. Karimi, M. Ghaedi, A. Asfaram, M.K. Purkait, Ultrasonic assisted removal of methylene blue on ultrasonically synthesized zinc hydroxide nanoparticles on activated carbon prepared from wood of cherry tree: experimental design methodology and artificial neural network, J. Mol. Liq., 229 (2017) 114–124.
[39]
[40] T.P. O'Connor, J. Mueller, Modeling competitive adsorption of chlorinated volatile organic compounds with the Dubinin–Radushkevich equation, Microporous Mesoporous Mater., 46 (2001) 341–349.
[41] M. Ghaedi, A. Hassanzadeh, S.N. Kokhdan, Multiwalled carbon nanotubes as adsorbents for the kinetic and equilibrium study of the removal of Alizarin Red S and Morin, J. Chem. Eng. Data, 56 (2011) 2511–2520.
[42] M. Ghaedi, B. Sadeghian, A. Amiri Pebdani, R. Sahraei, A. Daneshfar, C. Duran, Kinetics, thermodynamics and equilibrium evaluation of direct yellow 12 removal by adsorption onto silver nanoparticles loaded activated carbon, Chem. Eng. J., 187 (2012) 133–141.
[43] M. Toor, B. Jin, Adsorption characteristics, isotherm, kinetics, and diffusion of modified natural bentonite for removing diazo dye, Chem. Eng. J., 187 (2012) 79–88.